Bouchy 2001 inspired precision plot.

Bouchy inspired precision plot

The RV precision will be analysed further in Chapter 8.

2.3.1 Spectral disentangling efforts

Binary

Some techniques .. ?

Chapter 3

Near-infrared spectroscopy

In this chapter the basics of spectroscopy will be laid out, with the difference between optical and infrared spectroscopy given. A summary of several high-resolution nIR spectrographs relevant to this thesis will end this chapter.

3.1 Spectrograph basics

A spectrograph is a instrument of measuring the electromagnetic flux as a function of wavelength. All spectrographs have a few basic components common to all. A simple diagram with the basic components is shown in Figure 3.1. The first is the telescope which is used to collect light and focus the image of the sky onto its focal plane. A slit (or an optical fibre[1]) is placed on the telescopes' focal plane to block all but the light from desired target. The light passing through the slit is diverging so a collimator is used turn the diverging light into a parallel beam. The dispersing element is next and is responsible for dispersing the light into its separate components. This can be either a prism, grating (or even both). Following the dispersive elements are the optics for the camera, used to focus the dispersed (but still fairly collimated) light onto the detector, commonly a two-dimensional array of light sensitive pixels situated at the focal plane. Usually several optical elements, both lenses and mirrors, are used in combination to meet the constraints of the design specifications.

Figure Figure 3.2 shows the schematic for 3 different dispersions mechanisms, the refraction of light due to a change (Snells law) a transmission grating and a reflection grating. The left hand picture depicts

---

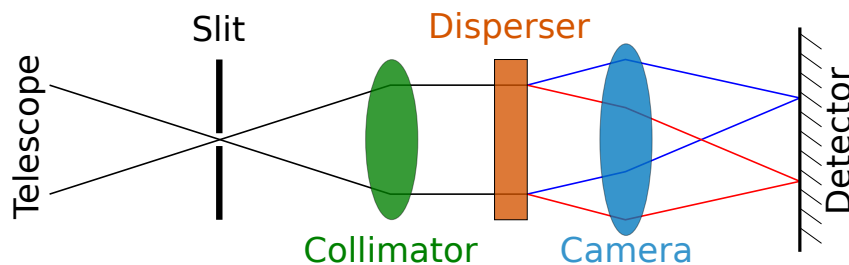[1]   Fibres allow for the spectrograph to be situated far from the telescope.

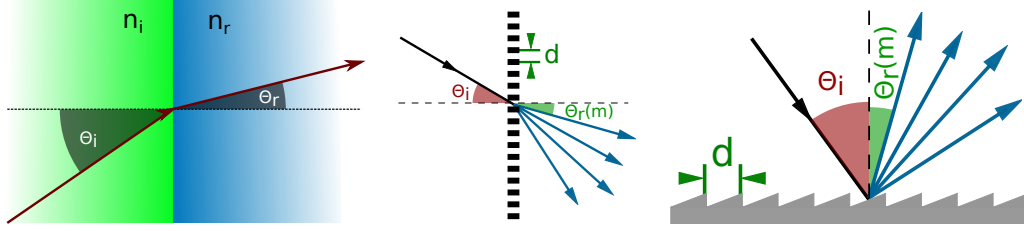**Figure 3.1:** Diagram of the basic components of a spectrograph.

Figure 3.2: Left: Dispersion at an optical boundary due to Snell's law. Middle: Dispersion from a transmission grating. Right: Dispersion from reflection grating.

in which refraction of light occurs when passing between two materials of different refraction index, n_i, and n_r. The angle of incidence *theta*$_i$ and angle of refraction θ_r relative to the normal (perpendicular) of the surface are related through Snell's law:

$$n_i \sin(\theta_i) = n_r \sin(\theta_r).$$

The index of refraction of a material is wavelength dependant the angle of refraction will be different for each wavelength, causing dispersion, like a prism.

The two dispersion gratings in Figure 3.2 are comprised of parallel narrow slits (transmission) or grooves (reflection), very close together. Diffraction from these slits/groves constructively and destructively interfere to create spectral orders that obey the grating equation:

$$m\lambda = d[\sin(\theta_i) \pm \sin(\theta_r)]. \tag{3.1}$$

Here m is the order number, λ the wavelength, d the spacing between the slits/grooves, and again θ_i and θ_r the incident and reflection angles respectively, relative to the normal.

This equation has degeneracy as different combinations of $m\lambda$ will be dispersed at the same angles. For instance the value $m\lambda$ for order m=54 at λ=2100 nm is that same as to order m=55 at λ=2061.8 nm. This degeneracy can be overcome in two ways, either apply a wavelength filter to specifically select only one order or by adding a cross-disperser. A *cross-disperser* is a second dispersive element oriented to disperse the orders perpendicular to the grating. This allows for multiple orders to recorded simultaneously on a two-dimensional detector, dramatically increasing the wavelength coverage. Echelle spectrographs are a special type of spectrograph, with a groove shape and orientation specifically for high reflection angles, and to observe at a high spectral order (high m) to achieve a high dispersion and high resolution.

Some important concepts for discussing spectrographs are the spectral resolution, resolving power, spectral coverage and spectral sampling. The spectral resolution, $\delta\lambda$, is smallest difference in wavelength able to be identified. It is related to resolving power which is defined as $R = \frac{\lambda}{\delta\lambda}$. The resolving power, R is colloquially also referred to as the resolution[2] The higher the resolution (resolving power), R, the smaller the $\delta\lambda$ that can be measured, leading to a high sampled spectral lines and more precise measurement. To be considered high-resolution, spectrographs typically have $R > 20\,000$, but the definition of "high" can differ between sub-fields of astronomy. The spectral coverage is the range of wavelengths able to be covered by the spectrograph, while the spectral sampling is the number of pixels required to sample the FWHM of the spectral lines. This value should be higher than 2 pixels per resolution element to satisfy

---

[2]   This document is no different.

Table 3.1: Properties of popular optical/IR detector materials. ε_g is the material band gap, the minimum excitation energy. λ_c is the cut-off wavelength corresponding to the maximum wavelength for each material. Common values for the detector operating temperature for the materials is given as T_{op}.

Material	Symbol	ε_g[eV]	λ_c[µm]	T_{op}[K]
Silicon	Si	1.12	1.1	163-300
Mer-Cad-Tel	HgCdTe	0.09-1.00	1.24-14	20-80
Indium Antimonide	InSb	0.23	5.5	30
Arsenic doped Silicon	Si:As	0.05	25	4

Nyquist sampling.

3.2 The detectors

The basic principles of spectroscopy are the same for optical and infrared are the same one difference is the design of the detector. Nowadays the most common type of detector are focal plane arrays, a two-dimensional of pixels located at the focal plane of the spectrographs camera. The purpose of the detector is to count the number of photons hitting each pixel in the array. This is achieved via the photoelectric effect on a crystalline structure, in which incident photons are transformed into electrons which can be recorded electronically. The energy necessary to excite an electron from the *valence band* to the *conduction band*, the characteristic band gap, is different for every material. Silicon is the best material for the detection of optical light (0.3–1.1 µm), while in the near-infrared (1–5 µm) two materials are used: Mercury-Cadmium-Telluride (HgCdTe) and Indium Antimonide (InSb). In the mid-infrared (5–20 µm) arsenic doped Silicon is used (Si:As).

Since photon energy is inversely proportional to wavelength[3], longer wavelength must have smaller band gaps. However, smaller band gaps are also more susceptible to electrons excited by thermal energy, known as the dark current. The dark current is dependant on detector temperature, the pixel size, quality of material and the materials cut-off wavelength λ_c. A summary of values for different material properties is given in Table 3.1.

The technologies for optical and IR detectors are very different. Figure 3.3 shows the main architectural difference between CCD and CMOS is given, with a very brief comparison between them below. Charge-Coupled Devices (CCDs) are used in the visible. Their use of silicon allows for the photo-induced electrons to methodically transfer the charge be from pixel to pixel along to one end. The electrons from each pixel pass to into amplifier to increase the signal, and then measured as a voltage difference with an analogue-to-digital converter (ADC). As the charge is shifted between pixels CCDs require high charge transfer efficiency (CTE) to not leave charge behind, which would be assigned to the incorrect pixels. CCDs have an almost 100% filling of photosensitive material. However the λ_c cut-off of silicon makes them unsuitable for the IR. More information on CCDs can be found in (Howell, 2000).

For IR the technology of choice is CMOS (Complementary Metal Oxide Semiconductor). Unlike CCDs, each individual pixel contains the circuity to read and amplify measure the charge in itself. Since the charge is read and amplified at each pixel there is no charge transfer between pixels and the readout is non-destructive. As a consequence, the same pixel can be read several times, averaging and thus reducing

---

[3] $E_{photon} = \frac{hc}{\lambda}$, where c is the speed of light, h is Plank's constant and λ wavelength.
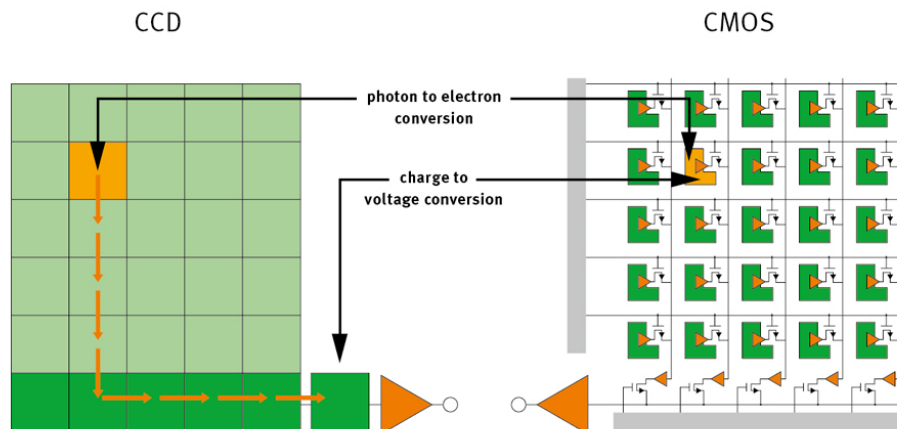
Figure 3.3: Schema differentiating CCD and CMOS detectors. In CCDs the charge is transferred to a specific pixel for measurement while in CMOS the charge is measured at the location of each pixel by individual amplifiers and ADCs. Credit https://automatie-pma.com.

the effective readout noise of each pixel. In theory, if one average N measurements before an observation (of a freshly reset detector), and N measurements of the observed charge after integration, the readout noise can be reduced by a factor of $\sqrt{(N)}$, referred to as *Fowler Sampling* (Fowler et al., 1990). Reading a CMOS detector is very versatile as it can be read in multiple ways, with the ability to randomly read any pixel at any time. The filling area of the photosensitive material is reduced in CMOS due to the presence of support architecture that is required for the circulation the top surface, partially blocking some of the incident light, reducing their efficiency.

As it is impossible to have every individual amplifier perfectly identical amplifier, there is a small sensitivity and gain difference between CMOS pixels, which are exposed by calibrating with a uniform light source. This contrasts with the one or few amplifiers used in CCDs, which lead to extremely homogenous amplification (as all pixels are amplified by the same amplifier). The CMOS circuitry is also intrinsically non-linear due to the changing capacitance as charge is collected. Irrespective if the charge is photo-induced or dark current, the circuitry measurement changes with the pixel charge level. This requires careful characterization of the non-linearities in the detector by calibrating its response to a uniform light source for a large range of integration times. For CRIRES there are a set of non-linearity coefficients that are applied while performing the flat-field corrections (see Section 5.1.1.2).

Other benefits of CMOS detectors are that they use lower power, and do not need a mechanical shutter (they can be reset electronically). While CCDs have been manufactured almost the same way for the last 40 years, CMOS technology is still advancing, partially driven by the consumer electronics market. Nowadays, most cellphone and laptop cameras use CMOS chips, helping to push investment in this technology. After the charge has been digitized into a number, the processes once again similar for both technologies.

3.2.1 Spectrograph cooling

Spectrographs must be cooled down for their detectors operate effectively as seen in Table 8.1. This is achieved by placing spectrographs and their supporting components inside a vacuum chamber, away

from all warm (radiating) component and precisely cooled[4] to low temperature. These are often referred to as cryostats. Modern instruments use closed-cycle refrigerators, with for example, helium as the working fluid to achieve very stable low temperatures inside the cyrostat. Providing a isolated, and stable environment for the spectrograph allows spectra science to be performed with the high precision possible, essential for detecting and charactering exoplanets.

Cooling plays two important roles for IR astronomy. Firstly, the thermal infrared emission from the components of the spectrograph surrounding the detector is reduced, diminishing the local background. Secondly, the detectors own thermally-generated background (dark current) is greatly reduced at low temperatures, leading to a gain in sensitivity.

Examples of two cryostat housings surrounding the spectrograph (but shown open) can be seen below in Figure 3.6.

3.3 CRIRES

CRIRES (Cryogenic InfraRed Echelle Spectrograph) is an ESO IR spectrograph that was mounted on the Unit Telescope (UT1, Autu) of the European Southern Observatory's Very Large Telescope (VLT) (Kaeufl et al., 2004) and available from April 2007 through July 2014[5]. The main optical elements consist of a prism pre-disperser and a 31.6 lines/mm echelle grating. The instrument provides resolutions up to 100 000 when used with a 0.2″ slit[6]. The wavelength range is 960–5200 nm with an instantaneous wavelength coverage of $\sim \lambda/50$. The spectra are imaged on a detector mosaic, consisting of four Aladdin III detectors (4096 × 512 pixel) in a row, with a gap of ~ 250 pixels between each chip. Adaptive optics (MACAO - Multi-Applications Curvature Adaptive optics) can be used to optimize the signal-to-noise ratio and the spatial resolution. Figure 3.4 displays the schematic representation of the CRIRES optical layout.

CRIRES lead the way for high-resolution spectrograph in the IR with a resolution higher than any of its predecessors, and unique capabilities, like adaptive optics. As with any new instrument there were several problems that affected CRIRES during its science operations. For instance there were several mechanical issues with the slit; the slit edges were not parallel and there were issues with precise and reproducible positioning. Other issues that require post observation correction such as detector glow, the odd even effect, and the wavelength calibration are detailed in Sections 5.1.1.1, 5.1.1.2 and 5.3.1.

3.4 The new generation

Building off the success of CRIRES several other nIR spectrograph have and being developed for different telescopes.

Their science goals for these instruments involve some or all of the following:

- Detecting low-mass planets in the habitable zone around late-type stars (M-dwarfs).

- Detecting and characterising the atmospheres of exoplanets.

- Observe and monitor clouds on brown dwarfs.

---

[4]   Temperature stability in the milli- Krange.
[5]   Note this PhD research began in October 2014.
[6]   The rule of thumb for the resolution of CRIRES is $R = 100\,000 \times \frac{\text{slit width}}{0.2''}$, with the slit width in arcseconds.
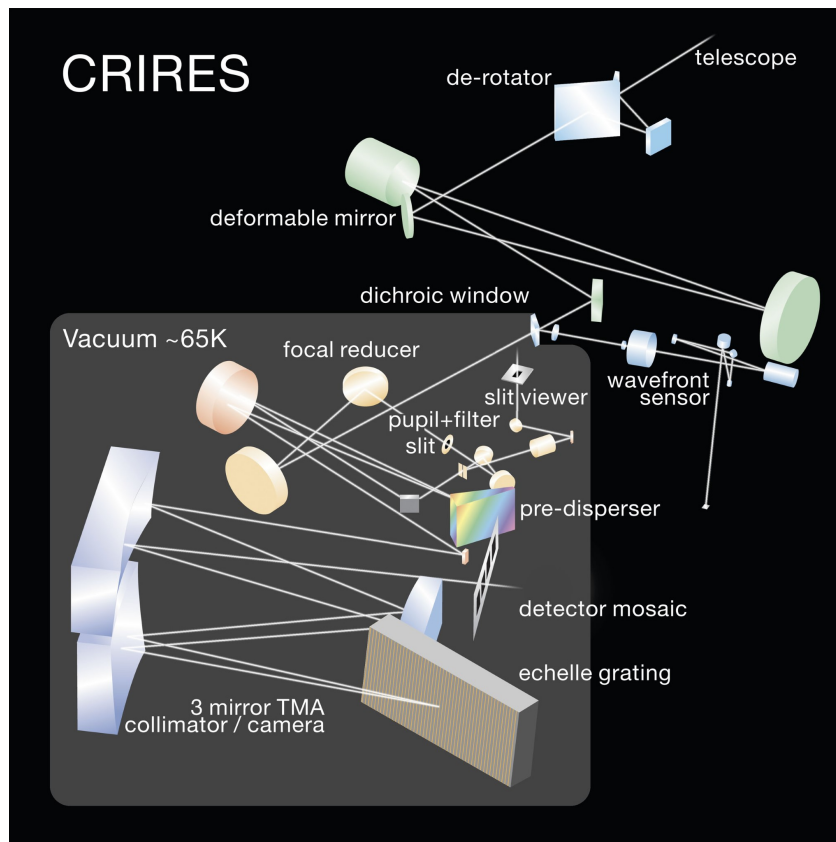
Figure 3.4: CRIRES layout schematic, taken from the CRIRES manual v93.

Table 3.2: A comparison between some high-resolution nIR spectrographs.

	CRIRES+	CARMENS (red)	NIRPS	SPIRou
Location	Paranal, Chile	Calar Alto, Spain	La Silla, Chile	Mauna Kea, Hawaii
Latitude	24°40′ S	37°13′ N	29°15′ S	19°49′ N
Available (* expected)	2019*	2016	2019*	2019*
Telescope diameter (m)	8.2	3.5	3.6	3.6
Wavelength Range (nm)	920–5200	960–1710	970–1810	980–2350
Resolution	50 000/100 000	80 400	75 000/100 000	70 000
RV precision (m s^{-1})	2–3	∼1	1	1
Operating Temperature (K)	70	140	80	77
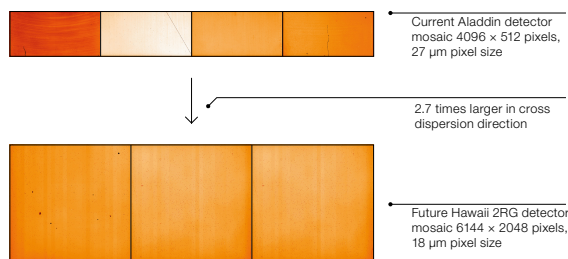
Figure 3.5: CRIRES detector focal plane array comparison with the new detectors. Credit Dorn et al. (2014).

- Analysing the spectra and atmospheres of cool stars.

- The origin and evolution of stellar magnetic fields (through spectropolarimetry).

A few points about some of the nIR instruments used in this work are detailed below with a summary also provided in Table 3.2.

> Is there other properties I should add to Table 3.2

3.4.1   CRIRES+

CRIRES was removed from operation in 2014 to undergo significant upgrades (Dorn et al., 2014). These include adding a cross-disperser to increase the simultaneous wavelength coverage by up to a factor of 10, improving the wavelength calibration by replacing the Th-Ar calibration lamp with a U-Ne lamp which has a richer set lines in the IR, and developing new multi-species gas absorption cells for the IR. The new upgrade adds the capability for spectropolarimetry using a polarization selective beam-splitter, in which the polarization of light in the spectrum can be analysed. The current detector mosaic will be replaced by 3 Hawaii 2RG detectors (6144 × 2048 pixels) at a pixel size of 18 μm. A comparison between the new and old detector size is shown in Figure 3.5. The new detector mosaic will not only provide a larger area but also lower noise, higher quantum efficiency, better cosmetic quality and much lower dark current [7]. The current estimate for the first light of CRIRES+ is first quarter of 2019.

---

[7]   https://www.eso.org/sci/facilities/develop/instruments/crires_up.html

3.4.2 CARMENES

CARMENES (Calar Alto high-Resolution search for M dwarfs with Exoearths with Near-infrared an optical Échelle Spectrographs) has been operating since 2016, performing an dedicated RV survey of ~ 300 late-type main-sequence stars with the goal of detecting low-mass planets in the habitable zone. It is mounted on the 3.5 m telescope at the Calar Alto Observatory in Spain, the light from the telescope is passes through a beam splitter and enters into two separate spectrographs, one in the optical (520–960 nm) and the other in the infrared (960–1710 nm). A library of single spectra of the M-dwarf targets CARMENES is monitoring was recently released in (Reiners et al., 2018).

3.4.3 NIRPS

NIRPS (Near-InfraRed Planet Searcher) is a nIR extension to the HARPS spectrograph on the 3.6 m telescope at La Silia, Chile. One of the most prominent spectrographs detecting exoplanets via a RV method. A replacement for the HARPS telescope adapter will be used to split the light and send the optical wavelengths to HARPS and IR to NIRPS via fibres. The adaptor also includes adaptive optics and a new calibration unit.

This will allow for the RV monitoring of cooler stars which emit more of their photons in the infrared but also have less stable optical spectra due to convection; infrared spectra are less affected by the stellar activity.

3.4.4 SPIRou

SPIRou (SPectroplorimètre InfraROUge) is another high-resolution nIR spectrograph that will be installed at the CFHT (Canada-France-Hawaii Telescope) in Hawaii. It will provide a spectrum covering from 950–2340 nm in a single exposure at a resolution of around $\sim 75\,000$. Like the other spectrographs detailed here it is built to obtain very high radial velocity accuracy, of the order meters/second over several year. It also includes spectropolarimetry, being able to derive the linear and circularly polarized state of the observed target.

A physical side-by-side comparison of the NIRPS and SPRIou spectrographs is shown in Figure 3.6, with NIRPS towards the front left.
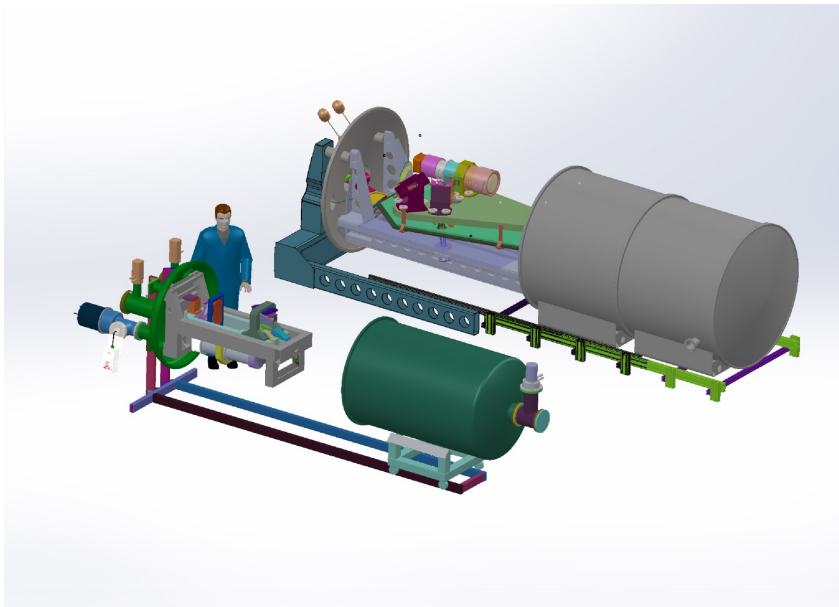
the Atmop-
shere in the
nir

Figure 3.6: Side by side comparison of the NIRPS and SPIRou spectrographs. NIRPS is the one in front on the left. Credit http://www.astro.umontreal.ca/nirps/.

Chapter 4

Atmospheres and Models

4.1 Earth's atmosphere, in the nIR

While the Earth's atmosphere is important life on Earth, it can be a nuisance for ground-based observations astronomical observations. While the atmosphere is mostly transparent in the visible, with only minor transmission and emission features, it is not uniformly transparent in the infrared.

As light form astronomical sources passes through Earth's atmosphere, the molecular species absorb specific wavelengths (corresponding to molecular rotational and vibrational energy levels) densely populating the nIR with absorption lines, commonly referred to as telluric absorption. Figure 4.1 contains the model telluric absorption spectrum for the atmosphere from 0.3–30 µm at $R \sim 10\,000$ from Smette et al. (2015). It clearly shows that there are regions where the atmosphere is mostly transparent (transmission of 1), with other wavelength regions (e.g. at 4.5 µm) that are completely opaque. Molecules which are the main contributors to the absorption are labelled.

The windows of transmission defined the location of photometric bands in the infrared, with the common ones listed in Table 4.1 (see e.g. Sterken et al., 1992; Binney et al., 1998). There are also variations on these bands for specific to different sites. These photometric bands are chosen for high average photometric[1] throughput, and do not consider the variable spectroscopic content inside the individual bands that becomes evident when observing at high resolution.

---

[1] Considering all photons in the band equally, regardless of wavelength (Very low resolution)

Table 4.1: Standard infrared pass-bands.

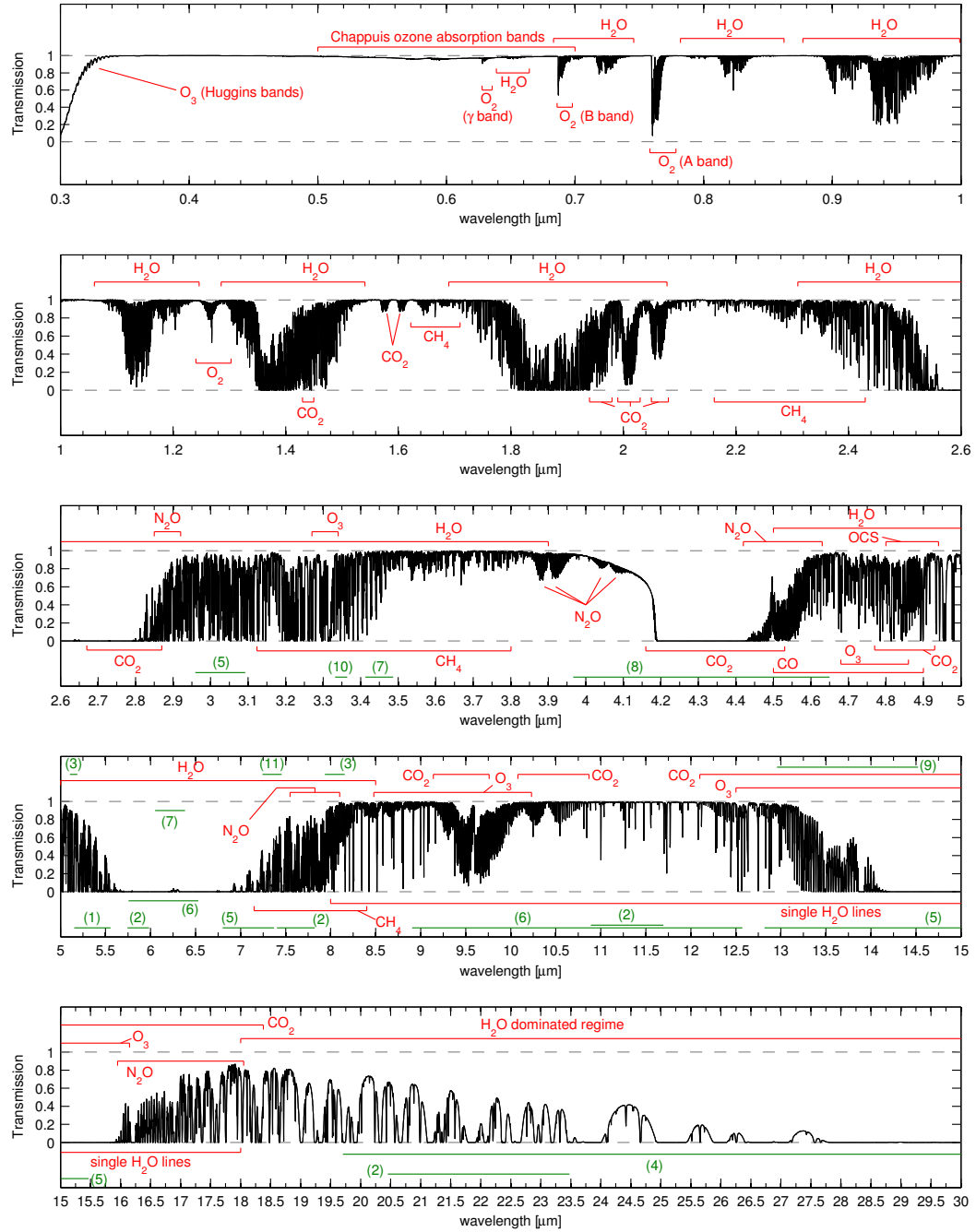| Band	Central wavelength [µm]	Bandwidth [µm]
Z	0.9	0.06
Y	1.05	0.12
J	1.25	0.38
H	1.65	0.48
K	2.2	0.4
L	3.5	1.2
M	4.8	0.6
N	10.6	2.5
Q	21	5.8

Figure 4.1: Telluric absorption map from 0.3–30 μm at $R \sim 10\,000$. The eight main molecules O_2, O_3, H_2O, CO, CO_2, CH_4, OCS, and N_2O contribute more than 5% to the absorption in some wavelength regimes. The red regions mark the ranges where they mainly affect the transmission, minor contributions of these molecules are not shown. The green regions denote minor contributions from the following molecules: (1) NO; (2) HNO_3; (3) COF_2; (4) H_2O_2; (5) HCN; (6) NH_3; (7) NO_2; (8) N_2; (9) C_2H_2; (10) C_2H_6; and (11) SO_2. Credit Smette et al. (2015, Figure 1).

The most prominent absorber in the infrared is water vapour (H_2O) which is a strong absorber defining the photometric bands as seen in Table 4.1. Water vapour is mostly concentrated in the lower 5 km, so infrared observatories are situated in dry places at high altitude. Even under ideal conditions the absorption of water vapour defines the IR bands. Other molecular species in the atmosphere are also important at various wavelengths, such as, CO, CO_2, CH_4.

When performing spectroscopy the spectrum of Earth's contaminates the spectrum of the intended target. In high-resolution spectroscopy the stellar and atmospheric lines can be resolved allowing for the identification and separation of the spectra. The removal or correction for the telluric lines is very important for accurate science, especially for detecting exoplanet atmospheres in which the species trying to be detected also reside in our atmosphere (Snellen et al., 2010; Brogi et al., 2014; de Kok et al., 2013).

The absorption of atmosphere is highly variable on many different time scales. The change in water vapour can occur rapidly over the course of the night while the concentrations of atmospheric constituents vary seasonal and even longer[2].

On top of this also the observational dependence on the airmass of the target. The airmass[3] is the relative path length through the atmosphere compared to zenith. The light of a target at a higher airmass passes through more of the atmosphere and is contaminated with deeper telluric liens.

Works such as Snellen et al. (2010), fit and remove the telluric variation during a series of continuous observations[4], to accurately remove the varying telluric lines and detect the absorption lines of exoplanet atmospheres.

4.2   Telluric correction

Typically atmospheric absorption correction has been performed by observing a standard star, a very hot (O or A-type), fast rotating star. These stars have minimal spectral features, so reveal the atmospheric absorption when observed. These standard stars need to be observed close in the sky and right before or after the science observation. To have similar atmospheric absorption to the science target. The science target can be corrected for the telluric line by division by the telluric standard star (e.g. Vacca et al., 2003). For high-resolution spectroscopy this technique is not sufficient to correct telluric with residuals greater than 2% remaining.

Recently synthetic modelling of telluric absorption has gained popularity with several works focusing on correcting telluric absorption with synthetic models (e.g. Bailey et al., 2007; Cotton et al., 2014; Seifahrt et al., 2010) and achieving better correction than the standard star method. Several different software available which usually build upon the standard line-by-line radiative transfer model code LBLRTM (Clough et al., 1995). Some examples are TelFit (Gullikson et al., 2014), and ESO's Molecfit (Smette et al., 2015) which both model and fit a synthetic absorption spectra to observations, where as TAPAS (Bertaux et al., 2014) just creates synthetic models based on atmospheric data for an observation (without fitting). The synthetic models at high resolution are very sensitive to atmospheric constituents, especially water vapour, and observing conditions such as the airmass.

Recently Ulmer-Moll et al. (2018) compared the telluric correction efficiency between TelFit, Molecfit, TAPAS, and the standard star method. They found that Molecfit and Telfit synthetic corrections lead to

---

[2]   For instance the increase in atmospheric CO_2 caused by anthropamorphic climate change has caused a 6% change to CO_2 line depths since 2000 (Smette et al., 2015).

[3]   Airmass $m = \sec\theta$ where θ is the zenith angle.

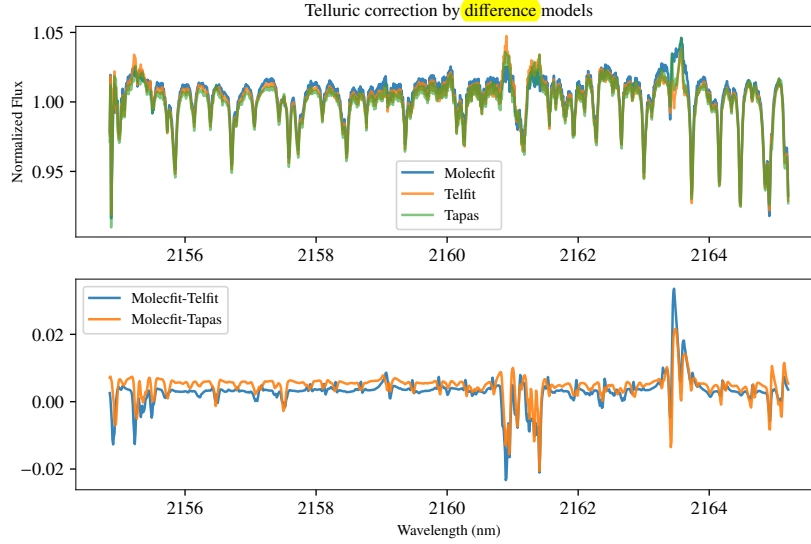[4]   51 spectrum of the same target in 180 minutes for Snellen et al. (2010)

Figure 4.2: CRIRES spectra with telluric correction applied using the Molecfit, TelFit and TAPAS. Top: The telluric corrected spectra. Bottom: Difference between the corrected spectra from the different methods.

smaller residuals for lines arising from H_2O, while the standard star method corrects for O_2 lines best. All methods (synthetic and standard star) result in a scatter inside the telluric lines of 3–7%. They also find that an observatory tailored atmospheric profile leads to reduced scatter inside telluric lines and that the correction performed better with lower precipitable water vapour.

As an example Figure 4.2 shows the telluric correction using the three different methods, Molecfit, TelFit and TAPAS[5], of a spectrum extracted for this work, detector #4 of observation HD 4747-1 (see Table 6.3). There are differences between the models of around 2% level, with the largest difference near the deep telluric line around 2163 nm.

Since sufficient telluric correction can be achieved through synthetic modelling, the observational requirement is halved as the standard star is not required, allowing more observing time for science. This is the case with the CRIRES observations analysed in this work. This work utilizes the synthetic spectra produced from TAPAS models are used correction the telluric lines in CRIRES spectra. These are detailed further below.

4.2.1 TAPAS web service

Telluric absorption spectra can be obtained with the TAPAS (Transmissions of the AtmosPhere for AStronomical data) web service[6] (Bertaux et al., 2014). TAPAS uses the standard line-by-line radiative transfer model code LBLRTM (Clough et al., 1995) along with the 2008 HITRAN spectroscopic database (Rothman et al., 2009) and ARLETTY atmospheric profiles derived using meteorological measurements from the ESPRI data centre[7] to create telluric line models.

The ARLETTY atmospheric profiles have a 6 hour resolution, so there may be a slight difference between the actual profile at the time of observation.

---

[5]   Performed here by Solène Ulmer-moll.
[6]   http://cds-espri.ipsl.fr/tapas
[7]   https://cds-espri.ipsl.upmc.fr

There are several parameters that can be submitted to the web service to define the requested telluric spectra, such as: target coordinates, date and time, location, spectral resolution, wavelength range and units choice observations, as well as the atmospheric profile and the choice of several atmospheric constituents to be included in the model spectra. TAPAS produces the telluric spectrum and sends a link to the results via email.

4.2.2   Requests for this work

Synthetic telluric absorption were requested from the TAPAS web service for this work. These were to match the CRIRES observations which are presented in Table 6.3.

The mid-observation time for each observation was used to request a synthetic spectra individually for each observation, with the ARLETTY atmospheric profiles and vacuum wavelengths selected. The telluric models were retrieved without barycentric correction to keep the telluric lines at a radial velocity of zero with respect to the instrument. For each observation one model was requested with all available atmospheric species present, convolved to a resolution of $R = 50\,000$, and a further two models without the instrumental profile convolution applied. For these two extra models, one contained only the transmission spectra of H_2O while the other contained contributions from the all other constituents except H_2O. This was to explore a known issue with the depth of H_2O absorption lines in the TAPAS models Bertaux et al. (2014) (see Section 5.3.2).

4.2.3   Issues with TAPAS

There are a number of issues encountered when using the TAPAS web service, mainly due to interaction with the website. Often their service were down for weeks at a time without any warning or notification. With this, time was wasted filling out and submitting a requests via the the web form without a response, or a returned spectra. There was also a variable level of success between different web browsers. A number of bug reports were submitted to the owners of the webpage without any acknowledgement.

The webpage is useful for quickly obtaining a small number of spectra but can be tedious for many spectra. For this work this was around upwards of 50 telluric spectra, (3 for each of the 17 observations). TAPAS offers the ability to request multiple spectra at a time but this was found to be unreliable when attempting to request more than four spectra in a single request.

A script[8] was created to automatically generate the data necessary to fill out a TAPAS request for each CRIRES observations. The script scanned the CRIRES header for information such as the mid-time of observations, target coordinates, slit width etc. and populated the XML request form provided by TAPAS. The script output is copied and pasted into the web browser for submission.

Trial and error was needed to understand all the XML form entries, such as the molecules requested and the atmospheric model to use (ARLETTY) and achieve a valid TAPAS request. The real issue was with the TAPAS ID number. Each TAPAS request has an ID number (which is provided with the email response). This ID number needs to be correctly set in the XML form before submission. This number is incremented by 1 with each submission but its initial value is unknown unless you made the very last request. If a submission is made via the XML request with the incorrect ID number a response will be returned with the correct ID number, but the failed request will be returned. This can then be used to increment the ID number by 1 and hopefully make a valid request. Unfortunately, if another user makes

---

[8]   Available at https://github.com/jason-neal/equanimous-octo-tribble/blob/master/octotribble/Tapas/

a TAPAS request between submissions the ID number will again be invalid. It is unknown if multiple transmission spectra could have been requested at the same time with the XML form.

There is another issue with a one hour time offset between the requested and the time returned by TAPAS. For instance if the requested time was for an observation at 0200h UTC then the transmission spectrum returned by TAPAS is for 0100h UTC. This changes the position of the target, the airmass and potentially the ARLETTY model used (6 hour time steps), affecting the strength of the telluric lines. It is tedious to remember to offset your input time by one hour to obtain the correct time, and slightly more work when you also have to adjust the date when going backwards past 0000h. When submitting the XML script the time that is returned is the time requested. Attempts were made to bring this issue to the attention of the TAPAS team in 2016 but as of August 2018 this issue is still present.

These issues need to be considered when requesting TAPAS spectra, adding unnecessary difficultly to the relatively simple process.

4.2.4 Telluric masking

The telluric spectra from TAPAS can not only be used for correcting individual spectra but are also easily used to create a wavelength mask telluric lines.For instance Figueira et al. (2016) and Artigau et al. (2018) use TAPAS spectra to mask out atmospheric lines deeper than 2% for computing the photon noise limited radial velocity precision. A telluric wavelength mask is similarly used in Chapter 8 when extending the analysis of Figueira et al. (2016). The telluric model used for this is an average of 52 TAPAS spectra (one per week in 2014), simulated at La Silla Observatory at an airmass of 1.2 ($z = 33.5^o$). This is to incorporate long-term variations of absorption over the year. Masking is applied by defining a cut-off line depth, typically 2%, at which to mask out any deeper lines.

Models help us to understand model, fit and predict the measurements and results and allow to compare to reality.

4.3 Synthetic Stellar models of cool stars

: Modelling of stellar structure, atmospheres and evolution is use to try and understand the observations, pieced together with several physical, chemical and hydrodynamical models. One output from these models is synthetic stellar spectra. These spectra can be compared to observed spectra to attempt to classify and understand the stellar populations. There is an ever evolving effort to improve these stellar models and synthetic spectra to better match the observations; incorporating more physics, chemical reactions and line lists, and using the latest element abundances. In this work extensive use of the PHOENIX-ACES models is made with some experimentation with the BT-Settl models. A collection of several theoretical stellar spectral libraries can be found at Spanish Virtual Observatory Theoretical Spectra Web Server.

The Kurucz (1979) models are popular synthetic models for stars ranging between G-O type with effective temperatures between 5 500–50 000 K. For cooler stars, M-dwarfs and even Brown Dwarfs the stellar models are based on the PHOENIX code (e.g. Hauschildt et al., 1997). Initially created for studying the ejecta of Novae it was *Extended* to low mass stars and Brown Dwarfs (Allard et al., 1995). The PHOENIX modelling code has evolved overtime incorporating new physical models to better explain the atmospheres. The *NextGen* models (Hauschildt et al., 1999) treated the stellar atmosphere as a gas

in chemical equilibrium, but the resulting spectra for very low mass stars was poor due to no treatment of dust in the stellar atmospheres.

The (Allard et al., 2001) *COND* and *DUSTY* models investigate the both extreme limits of clouds in the atmospheres of cool stars. They include condensation physics (Gibbs free energy, gas partial pressures etc.) into the chemical equilibrium model, as well as the optical interaction of light with the dust/condensates (dust opacities and scattering). The *DUSTY* models simulate 'inefficient/no settling' where condensation/dust forms and stays in the atmosphere and it affects the spectrum through the dust opacities. At the other extreme the *COND* models ignore the dust opacities and simulate 'efficient settling', in which all the condensates and dust clouds fall below the spectrum forming region.

The treatment of clouds and dust is important for the modelling of low mass stars and Brown Dwarfs. The *DUSTY/COND* models are similar above 2600 K but below this temperature they diverge below this temperature due to the crystallization of silicates in the atmosphere (Allard et al., 2001). These are only a few of the physical consideration implemented in the synthetic models. The other notable changes in the name convention for the synthetic spectra are due to use of specific line lists. The models beginning with AMES use the NASA-AMES H_{20} and TiO line lists, while the BT models use the Barber et al. (2006) H_2O line list. Between models improved solar abundance measurements are also implemented (Asplund et al., 2009).

In this work synthetic spectral from the PHOENIX-ACES and to a lesser extent the BT-Settl stellar models are used. These are further evolutions of the *DUSTY/COND* models and are detailed below.

Both sets of synthetic models do not handle the affects of radiation from a neighbouring star, which may have an affect on the BD companions studied here.

4.3.1 PHOENIX-ACES models

The PHOENIX-ACES models (Husser et al., 2013) are a descendant fo the *COND* models. They include condensation in equilibrium with the gas phase while ignoring dust opacity and any mixing or settling which is important for cooler atmospheres. As such the PHONEIX-ACES models are restricted to $T_{eff} > 2300$ K as the treatment of dust/clouds is not handled. It uses the most recent version (16) of the PHOENIX code and is suitable for the spectra of cool stars. THE PHOENIX-ACES models uses the Astrophysical Chemical Equilibrium Solver (ACES, Barman 2012) new in version 16 of PHOENIX to perform state-of-the-art treatment of the chemical equilibrium. It also adds parametrisations for the mass and mixing-length, and uses the solar abundances of Asplund et al. (2009).

As noted in (Husser et al., 2013) there are significant differences between the spectra from PHOENIX-ACES and previous PHOENIX model spectra. For instance the equation of state solver ACES strongly affects the stellar structure and different line and molecular band strengths. Unfortunately there are several changes introduced with PHOENIX-ACES making it difficult to distinguish and quantify the different effects.

The full parameter grid space of the pre-computed PHOENIX-ACES spectra is given in Table 4.2 although this full range is not utilized in this work. This work uses models below >7000 K with no α variation. The spectral sampling of the grid is are $R \approx 50\,000$ for 300–2500 nm, covering the wavelengths used here.

The lower temperature limits of this library limits the stellar mass to the highest mass BDs or higher. For example a $T_{eff} = 2\,300$ K corresponds to a BD with $M \sim 84$ M_{Jup} at 5 Gyr from the Baraffe et al.

Table 4.2: Full parameter space of the PHOENIX-ACES spectral grid. Reproduced from Husser et al. (2013).

	Range	Step size
T_{eff} [K]	$2\,300 - 7\,000$	100
	$7\,000 - 12\,000$	200
logg	$0.0 - +6.0$	0.5
[Fe/H]	$-4.0 - -2.0$	1.0
	$-2.0 - +1.0$	0.5
α/Fe	$-0.2 - +1.2$	0.2
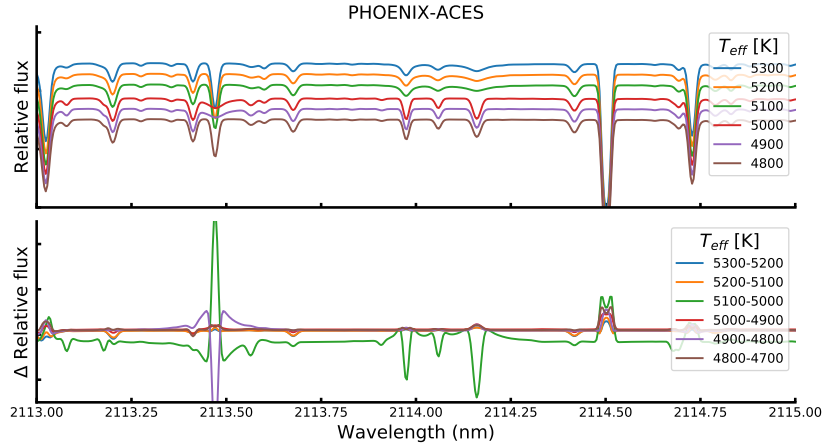
Figure 4.3: Top: Incremental PHOENIX-ACES model spectra between 4800–5300 K with logg=4.5 and [Fe/H]=0.0 fixed. Bottom: Difference in flux between successive models separated by 100 K. Apart from near absorption lines there a discontinuity in the flux of the PHONEIX-ACES modes between 5000 and 5100 K.

(2003) evolutionary models, (see Section 4.4).

While using the PHOENIX-ACES models a discontinuity in the stellar flux is observed between 5000 K and 5100 K. In Figure 4.3 several PHOENIX-ACES spectra in incremental steps are shown in a small wavelength range of 2113–2115 nm. The line profile seems to change suddenly between the model with 5000 K and 5100 K, causing a slight discontinuity in the models. This slightly impacts the use of these models while attempting χ^2 fitting in Chapter 7. The bottom panel shows the flux difference between models separated in temperatures of 100 K (one grid step). The difference between 5000 and 5100 K (green) is offset from the other model differences. This is potentially caused by the change in treatment of the model atmospheres at 5000 K. For instance Husser et al. (2013) mention that the reference wavelength defining the mean optical depth grid, is fixed to $\lambda_\tau = 1\,200$ nm for $T_{eff} > 5000$ K and $\lambda_\tau = 500$ nm for hotter stars in the PHOENIX-ACES modelling.

4.3.2 BT-Settl

The BT-Settl models (Allard, 2013; Baraffe et al., 2015), are an evolution of both the *DUSTY* and *COND* models. They are better suited for the entire range of BD temperatures down to 400 K, through hydrodynamical modelling of the mixing and settling of dust/clouds in the atmosphere of cool dwarfs **3d**

Table 4.3: Full parameter space of the BT-Settl (CIFIST2011_2015) spectral grid Baraffe et al. (2015).

	Range	Step size
T_{eff} [K]	$1\,200 - 7\,000$	100
logg	$2.5 - 5.5$	0.5
[Fe/H]	$0 - 0$	-
α/Fe	$0 - 0$	-

hydrodynamical modelling ....

They work on the version 15.5 of the PHOENIX code.

They are also suppose to have matching spectra on the range nIR-IR wavelengths (**allard...**).

In this work the BT-Settl models used did not go lower than the PHOENIX-ACES limit of 2300 K, but they were available if needed. Above this temperature there are some difference observed between the two models but their spectra are fairly similar at 2100-2160 nm used here.

The BT-Settl are generally more difficult to work with (in comparison to PHOENIX-ACES). The most recent BT-Settl spectral library designated CIFIST2011_2015[9] (Baraffe et al., 2015) includes newer Caffau et al. (2011) solar abundances and is combined with evolutionary modelling. It is available in a fits format which is easier to use. The parameter range available from the pre-computed library is given in Table 4.3.

Use multirow

4.3.3 Model access

The pre-computed synthetic spectral libraries for the PHOENIX-ACES models Table 4.2 are easily obtainable from http://phoenix.astro.physik.uni-goettingen.de/.

Pre-computed models for the BT-Settl and other PHOENIX spectra can be found at https://phoenix.ens-lyon.fr/Grids/ while A simulator is also available to generate BT-Settl spectra or other PHOENIX spectra from Allard France at phoenix.ens-lyon.fr, for specific parameters or abundances.

The spectral model libraries were downloaded using the above links and accessed using the useful "grid tools" interface provided in the *Starfish*[10] Python package (Czekala et al., 2015). The "grid tools" enables the fast, efficient, and simple loading of stellar spectra for use in the simulation performed in this work. For instance a spectra from a given modelled can be loaded simply using the four values of identifying parameter values [T_{eff}, logg, [Fe/H], α].

4.3.4 Comparing models

Here a comparison between the PHOENIX-ACES and BT-Settl spectra is briefly given. Figure 4.4 shows the model spectral flux in the nIR range of 0.9–3 µm for three different stellar temperatures: 5500, 4000, and 2300 K. At this large scale the spectra look fairly similar.

On closer inspection though the spectra are slightly different with the PHOENIX-ACES spectra having deeper absorption lines compared to the BT-Settl models, however they do appear to have most of the same absorption lines. This can be seen in Figure 4.5 which contains the PHOENIX-ACES and BT-Settl at two different regions in the nIR, 1013 nm and 2110 nm. Temperature of both models is 4300 K

---

[9] https://phoenix.ens-lyon.fr/Grids/{BT-Settl}/CIFIST2011_2015/
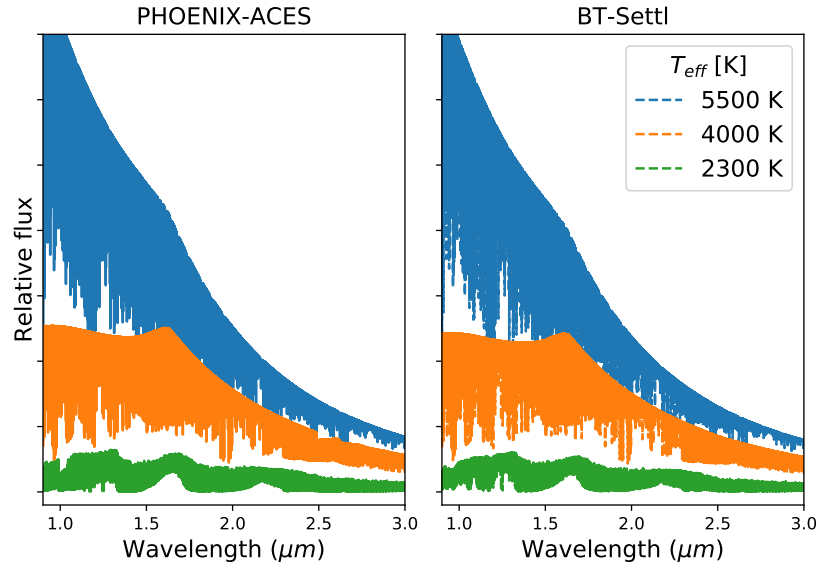[10] https://github.com/iancze/Starfish

Figure 4.4: PHOENIX-ACES (left) and BT-Settl (right) spectra in the nIR wavelength region for three different temperature stars, logg=4.5, [Fe/H]=0.
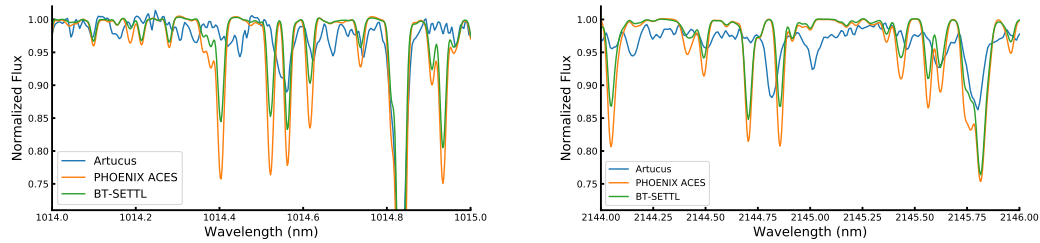

Figure 4.5

while the logg is 1.5 for PHOENIX-ACES and 2.5 for BT-Settl (closest available) and the models are convolved to R=100,000. This is in an attempt to match the parameters to the observations of Arcturus at R=100 000 shown blue. Cross-correlation and a Doppler shift has been used to align the model spectra to the observations. There is a striking difference between the models and observations which several lines present in the models that are not seen in the real observation, while a few lines observed that are not seen in the models. When the observed absorption lines do align with the models the is a difference in the depth of the lines. These difference are shown at two different wavelengths and reveal that there is still room for improvement in the synthetic models to match observed spectra in the nIRand at high resolution.

A further example of this is shown given in Figure 7.4 in which the fitted model, dominated by a single PHOENIX-ACES model, is compared to the observed CRIRES spectra. This caused issues with the fitting procedure in Chapter 7.

4.4 Evolutionary models

Modelling of the evolution of a star, from birth thorough its journey on the main sequence until its death as it slowly cools as a dwarf or explodes as a super-novae, is important for understanding how the observable properties (temperature, photometric colours) change over time. The main factor for the fate and evolution rate is a stars mass, with large stars evolving quickly and dying explosive deaths while low mass stars sustain fusion for several orders of magnitudes longer. Brown Dwarfs do not have enough mass to achieve stable hydrogen fusion and slowly cool down over their lifetime.

This work uses stellar evolutionary models of Baraffe et al. (2003) and Baraffe et al. (2015) to estimate the properties of the giant planets, brown dwarfs and low-mass stars given the mass and age. The models range in mass between 0.0005–1.4 $M_\odot$ and ages 0.001–10.0 Gyr of which span temperatures sim100–6000 K. Stellar/BD properties such as T_{eff}, logg, radius, and absolute magnitudes in different photometric bands can be determined from the tables given by the evolution models.

4.4.1 Estimating Companion-host Flux ratio

In order to visually or spectroscopically detect binary or planetary companions it is helpful to calculate the flux/contrast ratio between the host and companion.

The companion-host flux or contrast ratio of the system can be estimated using:

$$\frac{F_2}{F_1} \approx 2.512^{m_1 - m_2}, \tag{4.1}$$

where m_1 and m_2 are the magnitude of the host and companion respectively.

The photometric apparent magnitudes for the host stars, m_1, in several wavelength bands are easily obtained through online catalogues such as SIMBAD (Wenger et al., 2000) or 2MASS (Skrutskie et al., 2006). However, the magnitudes of the companions, m_2, are not readily available as they have not been directly measured. The stellar evolution models of Baraffe et al. (2003) and Baraffe et al. (2015) are used to estimate the magnitude of the companion. A given companion mass, and a stellar age will uniquely identify a point in the Baraffe models which corresponds to a specific magnitude for the companion. The evolution tables are also interpolated to reach companion masses and stellar ages between the models provided.

In Table 4.4 the host-companion flux ratio estimates for the targets analysed in this work are presented. The K-band flux ratios are calculated to match the observed CRIRES spectra at 2.1 µm. The stellar ages used for the each system are given in Table 6.1 while the companion masses are given from Table 6.2. The age and companion mass are both used to obtain the absolute magnitude for the companions. For the companions in which only the minimum mass ($M_2 \sin i$) is known then the flux-ratio given will be the lower limit, or worst case scenario.

The magnitudes provided by SIMBAD are given in apparent magnitude, m, while the magnitudes in the evolutionary models are absolute magnitudes M. That is, the apparent magnitude that the star would have if it was observed at a distance of 10 parsecs (32.6 light-years). The apparent magnitudes of the hosts are converted to absolute magnitudes using $M = m - \mu$ where μ is the distance modulus:

$$\mu = 5 \log_{10}(d_{pc}) - 5. \tag{4.2}$$

Here d_{pc} is the distance to the object in parsec. The distance is obtained from the trigonometric parallax

Table 4.4: Estimated flux ratios given the companion mass (M_2 or $M_2 \sin i$) from Table 6.2.

Companion	Host m_K	π mas	Host M_K	Companion M_K	Estimated F_2/F_1 K-band	Estimated N_2/N_1 (noise ratio)
HD 4747	5.305	53.184	3.82	14.17	7×10^{-5}	76
HD 162020	6.539	32.410	4.10	23.36	2×10^{-8}	1 615
HD 167665	5.038	32.014	2.60	13.21	6×10^{-5}	105
HD 168443b	5.211	25.208	2.35	42.19	1×10^{-16}	1×10^8
HD 168443c	5.211	25.208	2.35	29.55	1×10^{-11}	4×10^5
HD 202206B	6.485[a]	21.726	3.04	21.63	4×10^{-8}	1 586
HD 202206c	6.485[a]	21.726	3.04	45.63	9×10^{-18}	2×10^7
HD 211847B	7.018	20.489	3.50	8.40	0.011	14
HD 30501	5.525	49.081	3.96	10.38	0.003	27

[a] Magnitude from 2MASS catalogue instead of SIMBAD.

π using the formula $d(pc) = 1/\pi(arcsec)$, with the parallax in arcseconds[11]. In this work the recent high-precision parallax measurements from GAIA are used Collaboration et al. (2018).

From the flux ratio the noise ratio between the host and companion can also be calculated in a similar way using the equation $N_2/N_1 = \sqrt{2} \times \sqrt{F_1/F_2}$.

this section is completed i think

4.4.2   Baraffe tables

A simple tool[12] was created to calculate/estimate the host-companion flux ratio using the Baraffe et al. (2003) and Baraffe et al. (2015) evolution tables. Given the name of the target star, the mass of a companion and the stellar/system age the tool determines the flux ratios in the available spectral bands. The tool uses the targets name to query *astroquery* package the SIMBAD database to obtain the stellar properties, specifically the flux magnitudes and parallax. It then interpolates the Baraffe tables to the desired companion mass and age, calculating and returning values for all parameters of the companion given in the tables (e.g. T_{eff}, logg, $R/R_\odot$). The stellar magnitudes are converted to absolute values using Equation 4.2 and the flux ratios computed using Equation 4.1.

An extension of this tool is that can be used to perform the reverse calculation also. That is, given the target name, age and flux ratio in a given band it can estimate the mass of the companion mass using the evolution tables.

This section is completed I think

---

[11]   Most parallax values e.g. GAIA are tabulated in milliarcseconds (mas). Therefore it is important to remember to convert the parallax to arcseconds first, to avoid embarrassing calculation errors!

[12]   Available at https://github.com/jason-neal/baraffe_tables